

Electronic Supplementary Information
for
**Mapping the transition to superwetting state for nanotextured surfaces templated from
block-copolymer self-assembly**

Agnieszka Telecka^{1,#}, Nikolaj K. Mandsberg^{1,#}, Tao Li^{1,2}, Emil Ludvigsen¹, Sokol Ndoni^{1,3}, Rosa Di
Mundo⁴, Fabio Palumbo⁵, Jacek Fiutowski⁶, Serguei Chiriaev⁶, and Rafael Taboryski^{1,*}

¹Department of Micro- and Nanotechnology, Technical University of Denmark, DK-2800 Kongens Lyngby,
Denmark

²Department of Electronic and Electrical Engineering, University College London, WC1E7JE London, UK

³Center for Nanostructured Graphene, CNG, Technical University of Denmark, DK-2800 Kongens Lyngby,
Denmark

⁴Department of Chemistry (DICATECh), Politecnico di Bari, via Orabona 4, 70126 Bari, Italy

⁵Institute of Nanotechnology (NANOTEC), National Research Council, 70126 Bari, Italy

⁶Mads Clausen Institute, University of Southern Denmark, DK-6400 Sønderborg, Denmark

[*rata@nanotech.dtu.dk](mailto:rata@nanotech.dtu.dk)

[#]Agnieszka Telecka and Nikolaj K. Mandsberg contributed equally to this work.

Contents

S1: Optical transmittance spectra for structured and flat samples	S2
S2: Low-pressure Ar plasma activated PMMA surfaces	S2
S3: Roughness of unstructured PMMA surfaces activated by Ar plasma	S3
S4: Analysis of hemiwicking data.....	S4
S5: Geometry of nano-surfaces	S5
S6: Laplace pressure model.....	S6
S7: The “sunny side up” wetting model	S10
S8: Surface coatings.....	S13
S9: Young’s contact angle vs. surface free energy	S14
S10: Contact angle measurements.....	S16
References	S16

S1: Optical transmittance spectra for structured and flat samples

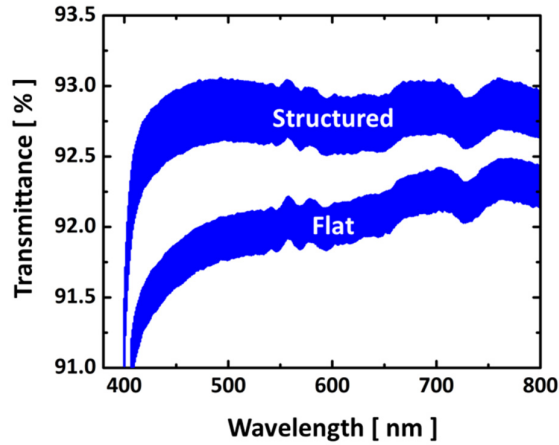


Figure S1. Transmittance measured by visual light spectroscopy. Traces show transmittance as a function of wavelength. Topmost trace is for a sample nanostructured on one side, while the bottommost trace is for the corresponding unstructured flat sample. The structured sample has $\sim 1\%$ higher transmittance in the visible spectrum. The width of the curves corresponds to $\pm SD$ from nine samples. The PMMA samples block light for wavelengths below ~ 400 nm.

S2: Low-pressure Ar plasma activated PMMA surfaces

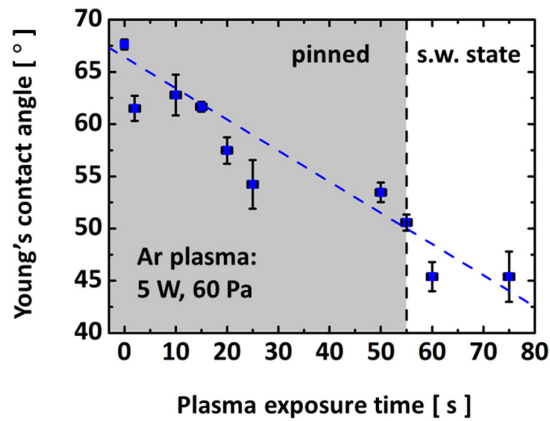


Figure S2. Calibration of the plasma exposure time. Young's contact angle as a function of Ar plasma exposure time. Dashed line is a linear fit to the data, with slope (-0.30 ± 0.03) $^{\circ}/s$, and y-axis intersection $(66.5 \pm 0.8)^{\circ}$.

Table S1. The relative signal content of C4 (C(O)-O) and C3 (C-O) in XPS spectra of pristine and Ar plasma treated PMMA surfaces (Ar plasma: 5W, 60 Pa, 70 s, ~ 2 h after plasma activation) . Uncertainties, obtained from residuals between Gaussian fits and data, are smaller than the significant digits shown.

	Untreated	Ar plasma treated
C4/total signal	18 %	22 %
C3/total signal	18 %	19 %
C4/C3	1.0	1.2

S3: Roughness of unstructured PMMA surfaces activated by Ar plasma

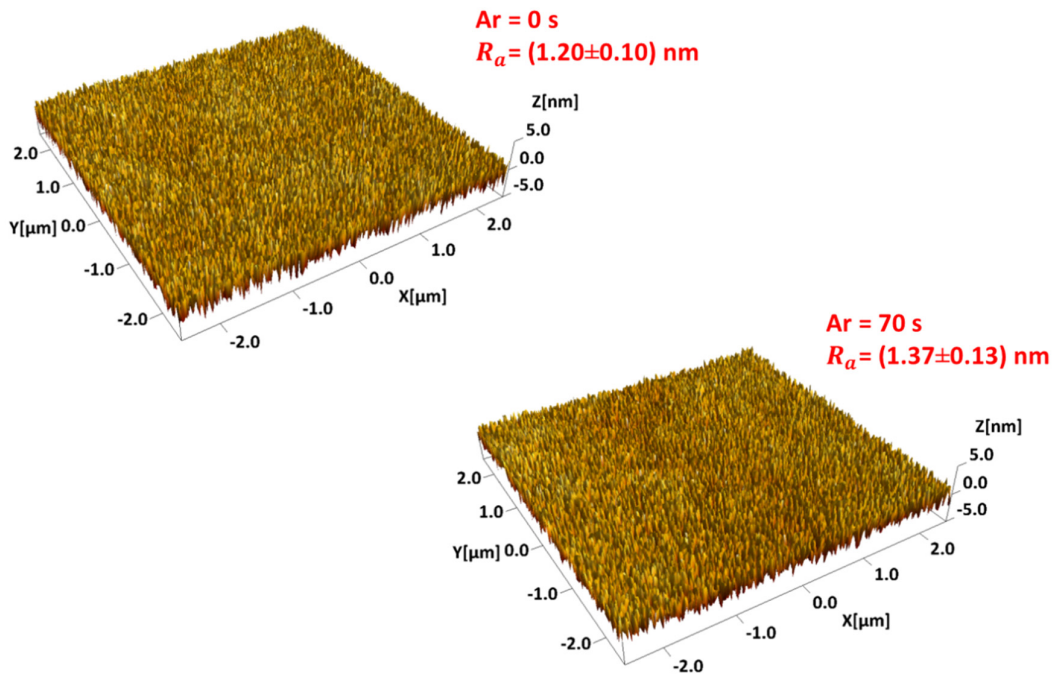


Figure S3. AFM 3D scans of pristine flat PMMA surface and 70 s Ar plasma treated flat PMMA surface. Arithmetic mean deviation R_a figures are given for both surfaces.

S4: Analysis of hemiwicking data

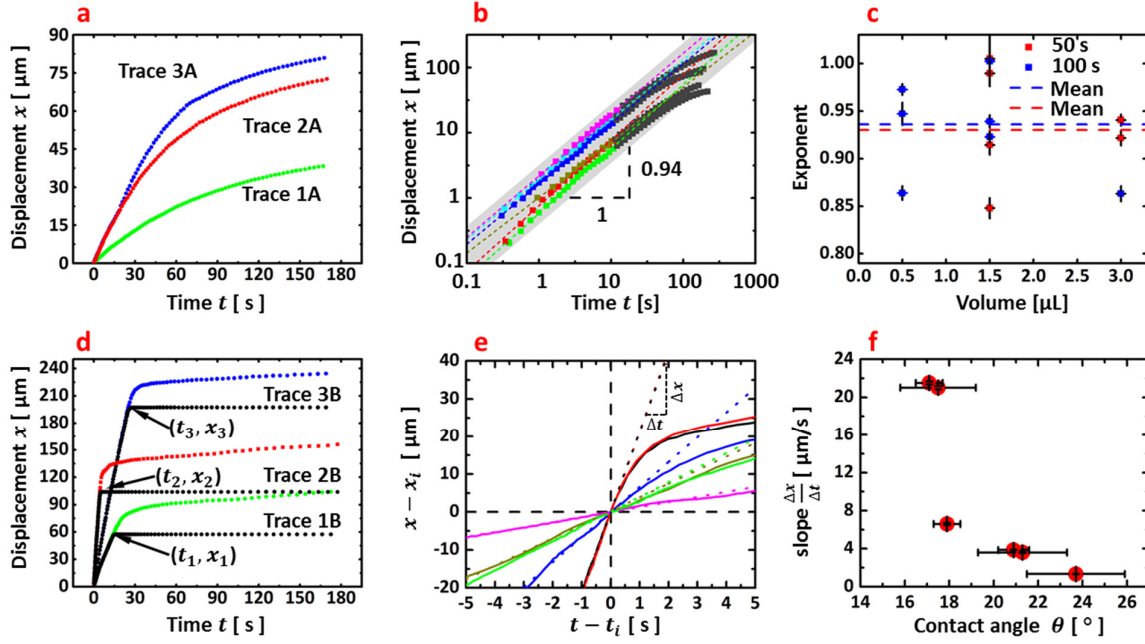


Figure S4. Data analysis for the three-phase-line propagation and the hemiwicking flow. **a:** Three examples of droplet propagation data obtained for samples exposed to 50 s of Ar plasma. **b:** A log-log plot for all 50 s Ar plasma data. Droplet displacements, x as functions of corresponding displacement times. The straight dashed lines show linear fits to the curves for times < 10 s. The average exponent 0.94 is also indicated. **c:** Summary of all exponents, both for 50 s and 100 s Ar exposure, plotted as a function of dispensed droplet volume. We see that all exponents fall in the range $[0.85; 1.00]$. **d:** Three examples of droplet propagation data obtained for samples exposed to 100 s of Ar plasma. The black curves represent radial displacement of the macroscopic droplet front, while the colored curves represent the nano-wicking flow. Times and positions when the macroscopic droplets stop is indicated for all three curves. **e:** The nano-wick displacement subtracted the corresponding macroscopic droplet standstill time and position. The macroscopic droplet propagation is omitted in this plot as it coincides with the abscissa. The graph also shows linear fit lines to the data in the interval $[-5; 0]$ s extended to full axis limits. **f:** The slopes of the linear fits from panel **S4e** quantifying the nano-wick propagation speed as a function of the apparent contact angle. The contact angles were obtained from the measured droplet radii in the droplet standstill conditions and the dispensed droplet volume by solving **Equation S1**. Error bars for the contact angles are obtained by the standard method for error propagation from experimental uncertainties in dispensed droplet volumes. The base radius uncertainty was neglected due to its small size as compared to the volume error.

The relationship between contact angle θ and droplet base radius R for a spherical droplet having volume V_0 is given by:

$$R^3 = \frac{3V_0}{\pi} \left(\frac{\sin^3(\theta)}{2 - 3\cos(\theta) + \cos^3(\theta)} \right). \quad (\text{S1})$$

S5: Geometry of nano-surfaces

The roughness factor is defined as *the ratio of the real surface in contact with the liquid to its projection onto the horizontal plane*¹. For a hexagonal array of cylindrical pillars, the roughness factor is given by:

$$r_{cyl} = \frac{\frac{1}{2}\sqrt{3}a^2 + \pi dh}{\frac{1}{2}\sqrt{3}a^2} = \frac{\frac{1}{2}\sqrt{3}\left(\frac{a}{d}\right)^2 + \pi\left(\frac{h}{d}\right)}{\frac{1}{2}\sqrt{3}\left(\frac{a}{d}\right)^2}, \quad (\text{S2})$$

where a is the center-center inter-pillar pitch length for the hexagonal pillar array, d is the diameter of pillars, and h is the height of pillars. Assuming the pillars are capped with a hemisphere, we instead get:

$$r_{sp} = \frac{\frac{1}{2}\sqrt{3}a^2 + \pi d\left(h - \frac{1}{2}d\right) + \frac{1}{4}\pi d^2}{\frac{1}{2}\sqrt{3}a^2}. \quad (\text{S3})$$

Table S2. Dimensions and roughness factors of BCP nanopillar templated surfaces with and without SiO_x and W coatings and their associated experimental uncertainties.

	d [nm]	h [nm]	a [nm]	r_{cyl} ^a	r_{sp} ^b
BCP	55.1±1.6 ^c	55±5 ^d	73.3±1.1 ^c	3.0±0.2 ^e	2.5±0.2 ^e
BCP+SiO _x	66.0±1.4 ^c	66±5 ^d	74.0±2.1 ^c	3.9±0.3 ^e	3.2±0.3 ^e
BCP+W	58±2 ^c	58±5 ^d	73.5±0.9 ^c	3.3±0.1 ^e	2.7±0.1 ^e

^a Wenzel roughness factor calculated using **Equation (S2)**.

^b Wenzel roughness factor calculated using **Equation (S3)**.

^c SD, n=10 obtained from SEM images.

^d Estimated from tilted SEM and Helium-ion imaging.

^e Error calculated with the standard formula for error propagation for independent variables.

S6: Laplace pressure model

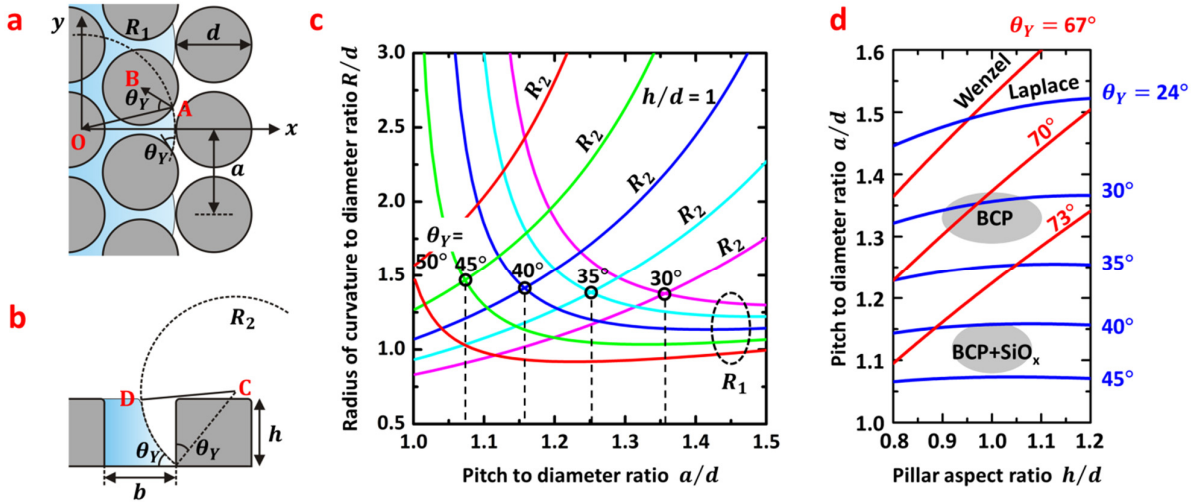


Figure S5. **a:** Schematic of top view of a pillar array comprised of cylinders. The lateral radius of curvature in the Laplace pressure is indicated in top view (R_1) together with the vectors \overline{AB} and \overline{AO} . The lattice constant a of the pillar array is shown together with the pillar diameter d . **b:** Schematic of cross sectional view along x -axis of the pillar array. The vertical radius of curvature (R_2) and cross section view of the pillar structure is shown together with the line segment CD . The height h of pillars, and b , the shortest distance between next nearest pillar rows, are also indicated. **c:** Examples of computed horizontal and vertical radii of curvatures, (R_1, R_2) in units of the pillar diameter as a function of the ratio between pitch and pillar diameter, a/d . The curves are plotted for the case of height to pillar diameter aspect ratio $h/d = 1$ and for various values of the Young contact angle θ_Y . The intersections between the R_1 and the R_2 plots indicate the zero Laplace pressure solutions. **d:** Red curves represent the Wenzel hemiwicking threshold. Wenzel curves for $\theta_Y = 67^\circ$, 70° , and 73° are plotted. The blue curves represent the Laplace hemiwicking condition obtained from a numerical solution of the equation $R_1 = R_2$, where the radii of curvatures are obtained from **Equations (S4)** and **(S5)**. Laplace model plots for $\theta_Y = 24^\circ$, 30° , 35° , 40° and 45° are shown. The relevant parameter space for the BCP structures replicated in PMMA, and the corresponding parameter space for the surfaces after the coating with an approximately 11 nm thick layer of SiO_x are indicated by the elliptical patches representing the uncertainty in the determination of the geometrical parameters (see **Table S2**).

For the sake of simplicity, we assume to start with that pillars are cylindrical. The model is based on a calculation of the Laplace pressures associated with the menisci for the hemiwicking liquid front as it passes a row of nano-pillars. Hence, we impose the condition that the Laplace pressure inside the liquid need to be negative in order to support the hemiwicking flows. If the Laplace pressure Δp inside the hemiwicking liquid becomes zero before the three-phase-line reach the next row of pillars, the wicking flow will stop, as the pillar array will effectively have a capillary stop action. The critical condition for hemiwicking is thus that the meniscus having radius R_1 at the bottom of the pillar array can reach the next row of pillars before the Laplace pressure Δp changes sign from

negative to positive. From inspection of the geometry in **Figure S5a,b** (see below for a more thorough derivation), the two radii of curvature can be expressed as

$$\frac{R_1}{d} = \frac{\frac{1}{4} \left(1 - \left(\frac{a}{d} \right)^2 - \left(\frac{b}{d} \right)^2 \right)}{\cos(\theta_Y) - \frac{b}{d}}, \quad (\text{S4})$$

and

$$\frac{R_2}{d} = \frac{\left(\frac{b}{2d} \right)^2 + \left(\frac{h}{d} \right)^2}{\left(\frac{2h}{d} \right) \cos(\theta_Y) - \left(\frac{b}{d} \right) \sin(\theta_Y)}, \quad (\text{S5})$$

where $b = \sqrt{3}a - d$ is the shortest distance between next nearest pillar rows. **Equation (S5)** is valid under the assumption that the liquid surface reaches the full pillar height at the narrowest gaps between the pillars as shown in **Figure S5a**. This assumption is satisfied for very dense pillar arrays, i.e. when $(a - d)$ is small compared to the pillar diameter d .² In **Figure S5c** we show the calculation of the radii R_1 and R_2 in units of the pillar diameter in the case of unity aspect ratio $h/d = 1$, whereas in **Figure S5d** we show numerical solutions for the Laplace hemiwicking condition (the blue curves) obtained from the condition $R_1 = R_2$ for the indicated values of Young's contact angle θ_Y . For a material having a given Young contact angle, superwetting will occur for the parameter space below a given trace. In the figure we also show the corresponding traces (red) indicating the critical Wenzel condition, $r_c = 1/\cos(\theta_Y)$. Likewise, according to the Wenzel condition, liquid will spread on the surface for the parameter space below the red traces for the respective Young contact angles. In **Figure S5d** we have also indicated the estimated relevant parameter space for the physical BCP structures replicated in PMMA, and the corresponding parameter space for the surfaces coated with an approximately 11 nm thick layer of SiO_x. The parameter ranges covered by the two elliptical shapes represent the physical variation or uncertainty in the determination of the geometrical parameters (see **Table S2**). From **Figure S5d** we see that the Wenzel threshold condition, $r > 1/\cos(\theta_Y)$ is more forgiving than the Laplace condition $\Delta p < 0$ as ranges of parameters for the ratio a/d and aspect ratio h/d will require a considerably lower Young contact angle θ_Y for the Laplace condition to be satisfied than for the Wenzel condition to be satisfied. For pristine uncoated BCP nanotextured PMMA samples having $\theta_Y = (68 \pm 2)^\circ$ and $r = 3.0 \pm 0.2$ (see **Table S2**), we would expect complete wetting behavior according to the Wenzel condition, while experimentally superwetting seems to occur only when θ_Y gets below $\sim 50^\circ$. One immediate implication from the Laplace pressure model is that no solution to the equation $R_1 = R_2$ seems to exist for θ_Y higher than $\sim 50^\circ$. This is shown in **Figure S5c**, where we plotted the radii of curvature as a function of the pitch to diameter ratio (a/d) for the case of $h/d = 1$. We see that when θ_Y approaches 50° there is no intersection between R_1 and R_2 for physically relevant parameters $a/d > 1$.

To derive the expression for R_1 in **Equation (S4)**, we consider **Figure S5a** and let point A be the intersection between the three-phase-line and the pillar boundary having the coordinates (x_1, y_1) and point B the center of the pillar with coordinates (x_0, y_0) in the reference system with origo in point O , such that $|\overrightarrow{AO}|^2 = x_1^2 + y_1^2 = R_1^2$, $|\overrightarrow{AB}| = d/2$, and $y_0 = a/2$. The angle θ_Y between vectors $\overrightarrow{AB} = \begin{pmatrix} x_0 - x_1 \\ y_0 - y_1 \end{pmatrix}$ and $\overrightarrow{AO} = \begin{pmatrix} -x_1 \\ -y_1 \end{pmatrix}$ can then be expressed by

$$\cos(\theta_Y) = \frac{\overrightarrow{AB} \cdot \overrightarrow{AO}}{|\overrightarrow{AB}| |\overrightarrow{AO}|} = \frac{\begin{pmatrix} x_0 - x_1 \\ y_0 - y_1 \end{pmatrix} \cdot \begin{pmatrix} -x_1 \\ -y_1 \end{pmatrix}}{R_1 d/2} = \frac{2R_1^2 - \{2x_0x_1 + y_1a\}}{R_1 d}. \quad (\text{S6})$$

By exploiting that point B is located on a circle having radius $d/2$ we get

$$(x_1 - x_0)^2 + (y_1 - y_0)^2 = \left(\frac{d}{2}\right)^2. \quad (\text{S7})$$

By inserting $x_1^2 + y_1^2 = R_1^2$ and $y_0 = a/2$ in **Equation (S7)** we get

$$R_1^2 + \left(\frac{a}{2}\right)^2 - \{2x_0x_1 + y_1a\} + x_0^2 = \left(\frac{d}{2}\right)^2. \quad (\text{S8})$$

From **Equation (S6)**, we isolate $\{2x_0x_1 + y_1a\}$ to insert into **Equation (S8)** and subsequently substitute $x_0 = R_1 - b/2$, where $b = 2a \cos(30^\circ) - d = \sqrt{3}a - d$ is the distance between next nearest pillar rows, we get

$$R_1(d \cos(\theta_Y) - b) = \left(\frac{d}{2}\right)^2 - \left(\frac{a}{2}\right)^2 - \left(\frac{b}{2}\right)^2. \quad (\text{S9})$$

By rearranging we finally get **Equation (S4)**.

Likewise to derive the expression for R_2 in **Equation (S5)** we exploit that the length of the line segment CD in **Figure S5b** equals R_2 but can also be expressed by

$$|CD|^2 = \left(\frac{b}{2} + R_2 \sin(\theta_Y)\right)^2 + (R_2 \cos(\theta_Y) - h)^2 = R_2^2. \quad (\text{S10})$$

Rearranging and cancelling terms we get

$$R_2(2h \cos(\theta_Y) - b \sin(\theta_Y)) = \left(\frac{b}{2}\right)^2 + h^2. \quad (\text{S11})$$

Finally by another rearrangement, we get **Equation (S5)**.

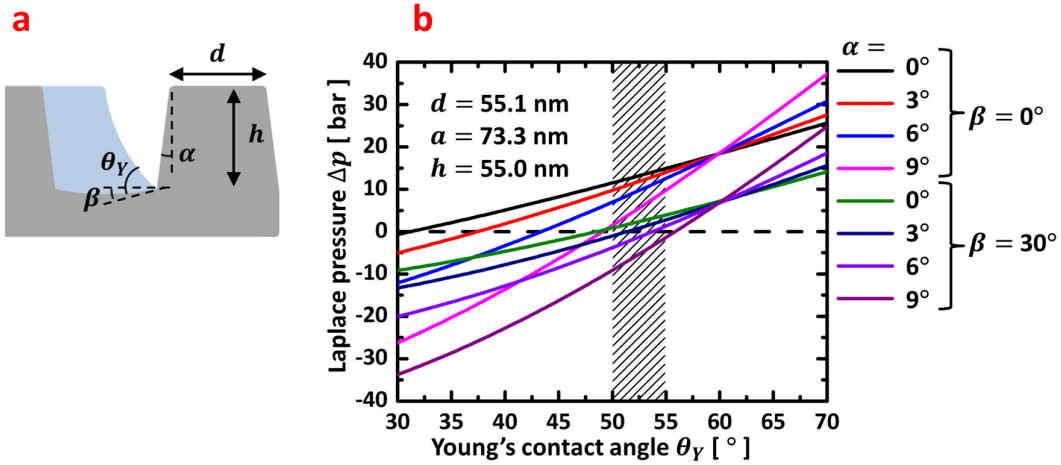


Figure S6. Corrections to the Laplace pressure model due to effects of tapered pillars (taper angle α) and sloped (angle β with horizontal) substrate bottom at the root of the pillars. **a:** Schematic of cross-sectional view along a symmetry-axis of the pillar array (corresponding to the view shown in **Figure S5b**, but here with sloped bottom and pillar taper). The height h of pillars, taper angle α , and slope angle β with horizontal are also indicated. **b:** Examples of computed Laplace pressure curves corresponding to the indicated values of (α , β). The curves are plotted for the measured values of lattice constant a , top pillar diameter d , and pillar height h . The shaded region indicates the experimentally determined range Young's contact angles, where crossover is observed between the superwetting, state represented by negative Laplace pressures, and the pinned state, represented by positive Laplace pressures.

To ease the harsh $\theta_Y < 50^\circ$ condition obtained above for cylindrical pillars placed on a perfectly planar substrate bottom, we only need to assume a sloped (angle β with horizontal) substrate bottom at the root of the pillars. Considering the fabrication by injection molding of the pillar-built surface, a sloped substrate bottom is moreover a more realistic geometry. This is the case as the governing angle in the derivation of R_2 is the angle to the horizontal direction, and hence a slope with angle β will have to be subtracted from θ_Y in the calculation of R_2 in **Equation (S5)**. Further as shown **Figure S6** a shift toward higher a/d occurs when having a small taper of the pillars. As it is the condition at the bottom of the pillars that govern the hemiwicking flow, whereas the pillar diameter is measured at the top of pillars, then for $h \approx d$, a small taper of the pillars corresponds to making the replacement $(a/d) \rightarrow (a/d)(1 + 2 \tan \alpha)^{-1}$ in **Equations (S4) and (S5)**, whereby the pillar array effectively gets denser. The transition from the pinned - to the superwetting state occurs when the Laplace pressure for the meniscus of the hemiwicking liquid front emerging between pillars changes sign from positive to negative. Hence, in **Figure S6b** we show how the Laplace pressure changes sign when Young's contact angle crosses the transition. The experimentally observed crossover Young contact angle for superwetting of $\sim 50^\circ$ - 55° can be obtained with e.g. $\alpha \sim 6^\circ$ and $\beta \sim 30^\circ$ for the measured geometrical parameters from **Table S2**. Although a precise measurement of the slopes was not possible due to lack of resolution, we found experimental support for the tapered pillar walls and sloped bottom in the SEM analysis (see e.g. **Figure 5b**).

S7: The “sunny side up” wetting model

The “sunny-side up” model of Ishino and Okumura³ based on initial experiments of Bico et al.⁴, with the yolk representing the sessile droplet, and the white representing the wicked water film (**Figure S7**), is here derived for a hexagonal array of pillars capped with oblate half-spheroids. The model is finally compared to contact angle data from **Figure 1a**.

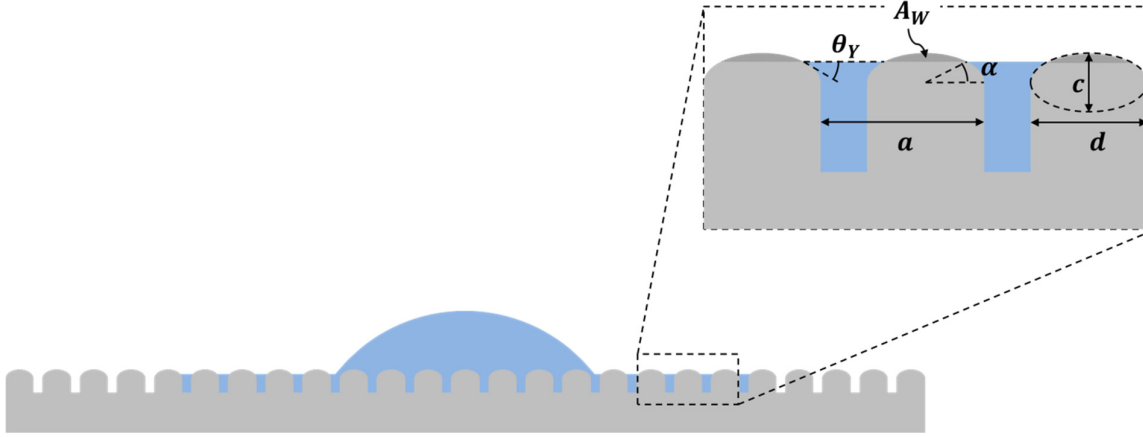


Figure S7. Sketch of the model. The drop is placed on a hybrid surface composed of a wicked water film and the dry pillar tops. Pillar tops are assumed to be capped with oblate half-spheroids.

Now following Miwa et al.⁵ and Whyman et al.¹ we can express the apparent contact angle θ for a small droplet in thermodynamic equilibrium sitting on a chemically heterogeneous rough surface comprised of the wicked water film and the dry pillar caps by:

$$\cos \theta = \left(\frac{A_W}{A_{hex}} \right) \cos \theta_Y + \left(1 - \frac{A_{WP}}{A_{hex}} \right). \quad (\text{S12})$$

With $A_{hex} = \frac{\sqrt{3}}{2} a^2$. Due to the dependencies of A_W and A_{WP} on θ_Y , we will see that θ becomes slightly more complicated than was the case for perfectly cylindrical pillars reported by Bico et al.⁴. The model corresponds to the well-known Cassie⁶ model for a chemically heterogeneous rough surface comprised of pillar caps with local contact angle θ_Y , and a wicked water film having contact angle 0.

We now turn to find the areas A_W and A_{WP} in **Equation (S12)**. The area of the oblate spheroid above the wicked water film, i.e. the dry area, is given by:

$$A_W = \int_{\alpha}^{\frac{\pi}{2}} 2\pi x \sqrt{\left(\frac{dx}{d\varphi} \right)^2 + \left(\frac{dy}{d\varphi} \right)^2} d\varphi, \quad (\text{S13})$$

where $(x, y) = \left(\frac{d}{2} \cos \varphi, \frac{c}{2} \sin \varphi\right)$. This area will contribute to a Wenzel-like roughness; hence the index “W” is used to designate this area. By introducing the eccentricity of the oblate spheroid, $\varepsilon = \sqrt{1 - \left(\frac{c}{d}\right)^2}$, we get

$$A_W = 2\pi \left(\frac{d}{2}\right)^2 \int_{\alpha}^{\frac{\pi}{2}} \cos \varphi \sqrt{1 - \varepsilon^2 \cos^2 \varphi} d\varphi, \quad (\text{S14})$$

where the angle α is a function of Young’s contact angle θ_Y and eccentricity ε through the relation $\tan \alpha = (1 - \varepsilon^2) \cot \theta_Y$. The projection of the dry area is given by

$$A_{WP} = \frac{\pi \left(\frac{d}{2}\right)^2}{1 + \frac{\tan^2 \alpha}{1 - \varepsilon^2}}. \quad (\text{S15})$$

For $\varepsilon \rightarrow 1$, the pillars become cylinders with completely flat caps and $A_W = A_{WP} = \pi(d/2)^2$, whereby also the dependence on θ_Y disappears as expected.

Next we plot our data from **Figure 1a** together with the contact angle obtained from **Equations (S12-S15)**. This is shown in **Figure S8**.

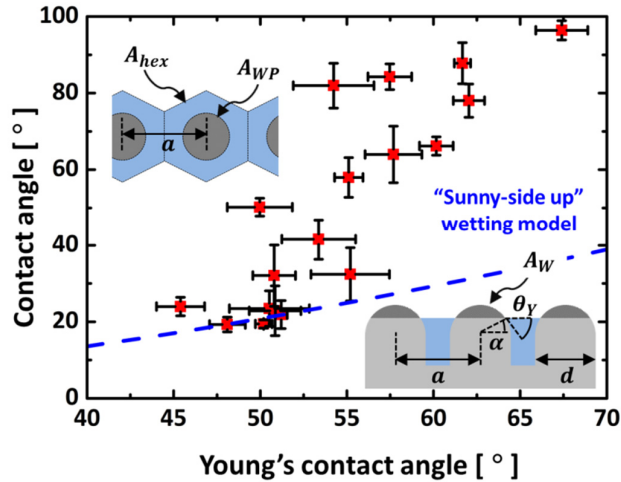


Figure S8. The data from **Figure 1a** plotted together with the contact angle θ obtained from **Equations S12-S15** with $\varepsilon = 0$, i.e. for a hemi-spherical cap. No adjustable parameters are used, as measured values $d = 55.1 \text{ nm}$ and $a = 73.3 \text{ nm}$ (found in **Table S3**) are applied in the computation.

In **Figure S8**, we plot only model data corresponding to $\varepsilon = 0$. For $\varepsilon \rightarrow 1$, the model is equivalent to the expressions of Bico et al.⁴ and Ishino and Okumura³, which for our data gives $\theta \approx 30^\circ$ at $\theta_Y \approx 40^\circ$. The dependence on cap eccentricity is, however, not a monotonic function, and yields a minimum contact angle for $\varepsilon \approx 0.75$. We see that the model can be used to predict an asymptotic value for low Young contact angles, i.e. for $\theta_Y \lesssim 50^\circ$, whereas for higher θ_Y the data begin to deviate substantially from the model. We interpret this deviation as a transition to the so-called pseudo-Wenzel state³, where the droplet leaves thermodynamic equilibrium.

S8: Surface coatings

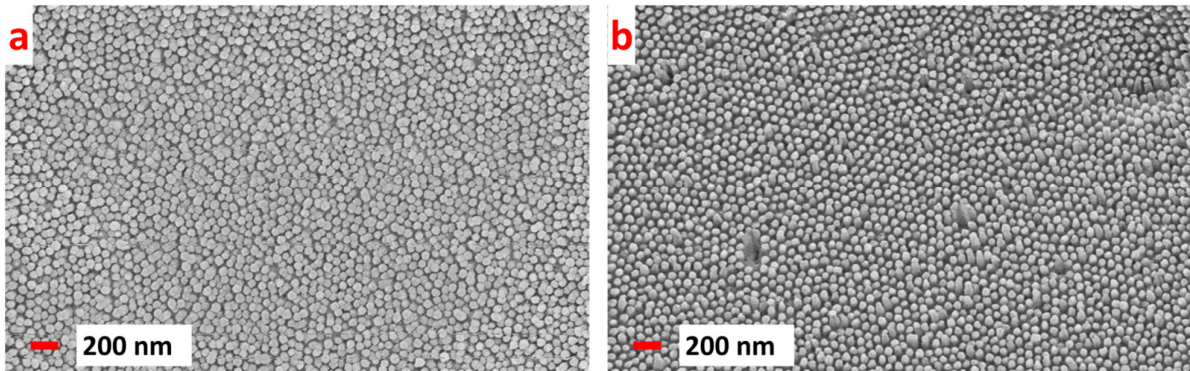


Figure S9. SEM image of PMMA nanotexture after coating with. **a**: ~ 11 nm of SiO_x and **b**: ~ 8 nm of W.

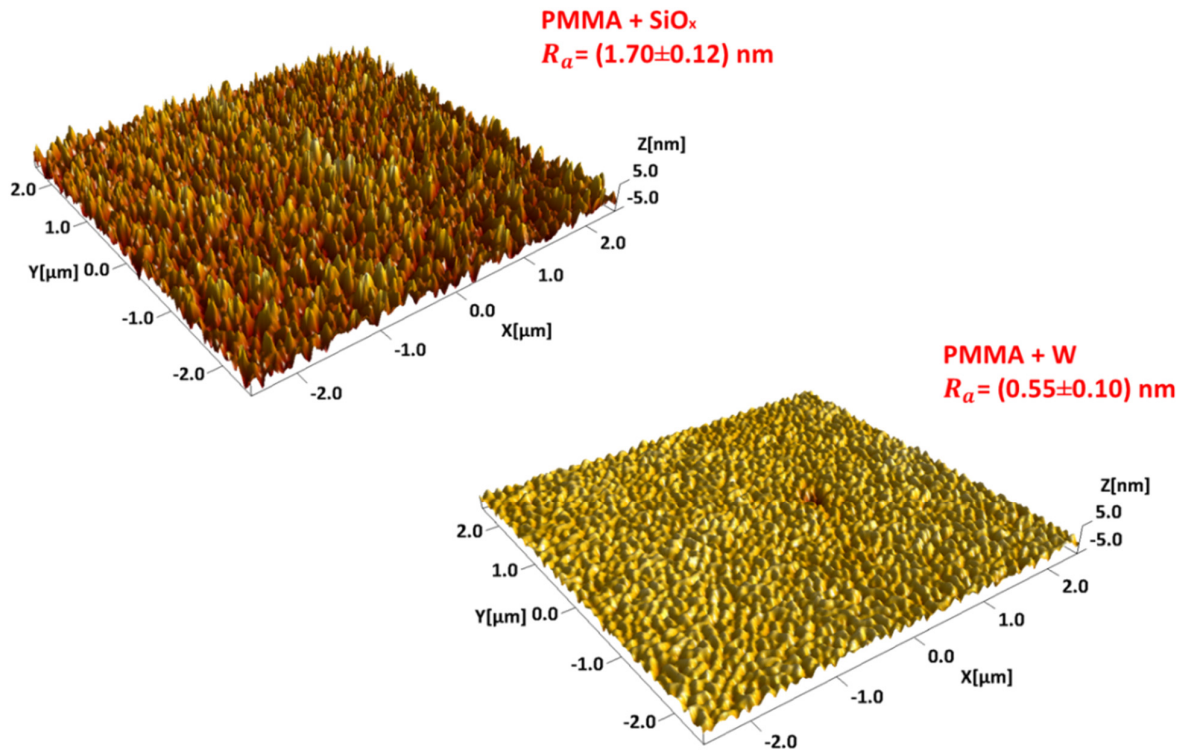


Figure S10. AFM 3D scans of pristine flat PMMA surface with SiO_x and W surface coating. Arithmetic mean deviation R_a figures are given for both surfaces.

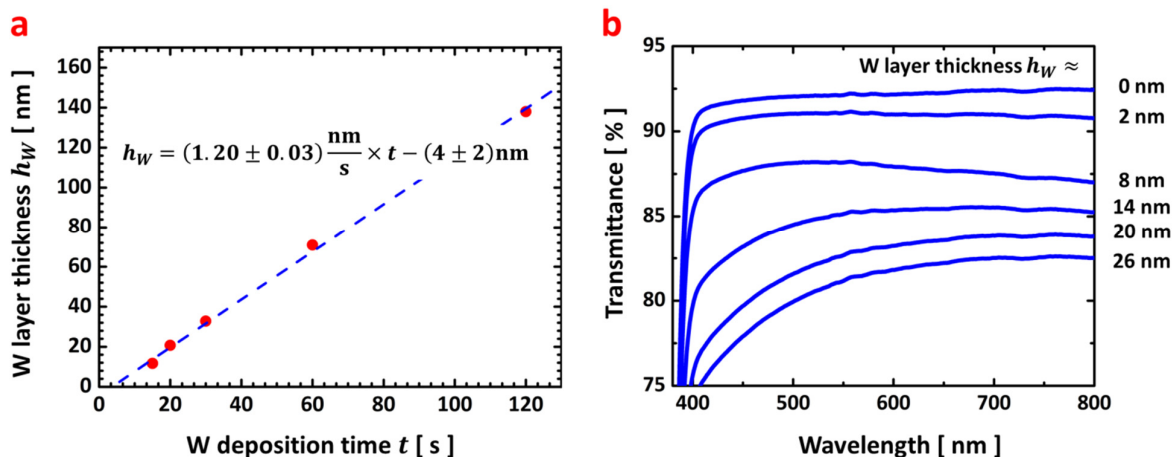


Figure S11. a: Thickness of the tungsten (W) layer measured (red dots) as a function of deposition time. A linear fit (blue dashed line) is shown. **b:** Transmittance spectra from PMMA samples with tungsten (W) coating. Traces show transmittance spectra for increasing W deposition time corresponding to increasing thickness of W.

S9: Young's contact angle vs. surface free energy

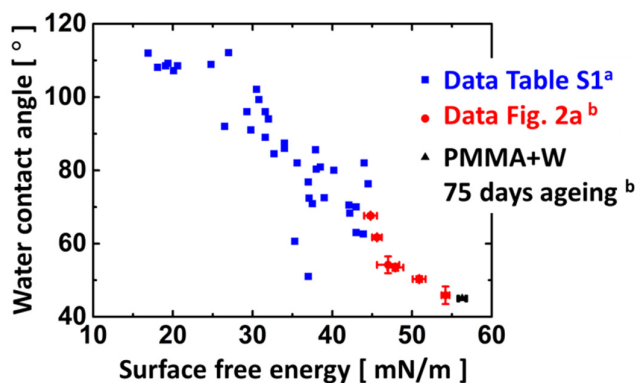


Figure S12. Contact angle as a function of material surface free energy. ^aData obtained from: https://www.accudynetest.com/polytable_03.html?sortby=contact_angle (accessed April 26'th 2018). ^bSD, $n = 5$, error calculated with standard method for error propagation.

Table S3. Surface free energy and the corresponding proxies for the Young contact angle of common polymers. Data obtained from https://www.accudynetest.com/polytable_03.html?sortby=contact_angle (accessed April 26th 2018).

Polymer name	γ [mN/m]	CA [°]
Polyvinyl alcohol (PVOH)	37.0	51.0
Polyvinyl acetate (PVA)	35.3	60.6
Nylon 6 (polycaprolactum, aramid 6)	43.9	62.6
Polyethylene oxide (PEO, PEG, polyethylene glycol)	43.0	63.0
Nylon 66	42.2	68.3
Nylon 77	43.0	70.0
Polysulfone (PSU)	42.1	70.5
Polymethyl methacrylate (PMMA, acrylic, plexiglas)	37.5	70.9
Nylon 12	37.1	72.4
Polyethylene terephthalate (PET)	39.0	72.5
Epoxies	44.5	76.3
Polyoxymethylene (POM, polyacetal, polymethylene oxide)	37.0	76.8
Polyvinylidene chloride (PVDC, Saran)	40.2	80.0
Polyphenylene sulfide (PPS)	38.0	80.3
Acrylonitrile butadiene styrene (ABS)	38.5	80.9
Nylon 11	35.6	82.0
Polycarbonate (PC)	44.0	82.0
Polyvinyl fluoride (PVF)	32.7	84.5
Polyvinyl chloride (PVC)	37.9	85.6
Nylon 88	34.0	86.0
Nylon 99	34.0	86.0
Polystyrene (PS)	34.0	87.4
Polyvinylidene fluoride (PVDF)	31.6	89.0
Poly n-butyl methacrylate (PnBMA)	29.8	91.0
Polytrifluoroethylene	26.5	92.0
Nylon 10,10	32.0	94.0
Polybutadiene	29.3	96.0
Polyethylene (PE)	31.6	96.0
Polychlorotrifluoroethylene (PCTFE)	30.8	99.3
Polypropylene (PP)	30.5	102.1
Polydimethylsiloxane (PDMS)	20.1	107.2
Poly t-butyl methacrylate (PtBMA)	18.1	108.1
Fluorinated ethylene propylene (FEP)	19.1	108.5
Hexatriacontane	20.6	108.5
Paraffin	24.8	108.9
Polytetrafluoroethylene (PTFE)	19.4	109.2
Poly(hexafluoropropylene)	16.9	112.0
Polyisobutylene (PIB, butyl rubber)	27.0	112.1

S10: Contact angle measurements

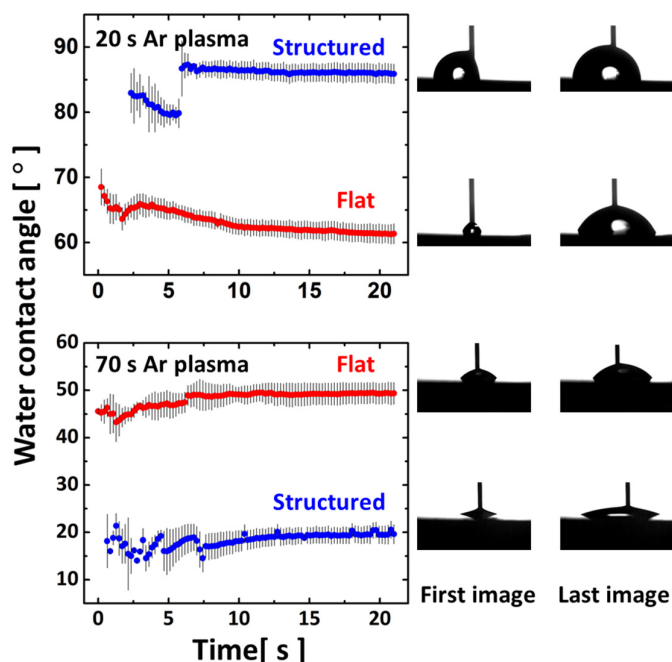


Figure S13. Contact angle measurements were done using the droplet inflation methods, where the capillary was left inside the droplets during the contact angle fitting. The droplets were slowly inflated with water to a total volume of $6.5 \mu\text{L}$. Data recorded during the first 10 seconds were typically corrupted by the presence of the inflation capillary and were discarded for contact angle determination. The figure shows the fitted contact angles as function of time during the inflation process for two representative datasets that were used in **Figure 1**; one set (upper panel) for the pinned state, where the structured surface has higher contact angle than the unstructured counterpart subjected to the same Ar plasma treatment, and another set (lower panel) for the superwetting state, where the contact angle for the structured surface was lower than for the corresponding unstructured one. Due to use of the inflation method, the recorded contact angles are interpreted as advancing contact angles. After having ensured that the fitting procedure converged, the last images were used for obtaining the advancing contact angles in **Figure 1**. The error bars represent the absolute value of the difference between the fitted contact angles from the left and the right sides of the droplet profiles.

References

1. G. Whyman, E. Bormashenko and T. Stein, *Chemical Physics Letters*, 2008, **450**, 355-359.
2. J. Kim, M. W. Moon and H. Y. Kim, *Journal of Fluid Mechanics*, 2016, **800**, 57-71.
3. C. Ishino and K. Okumura, *European Physical Journal E*, 2008, **25**, 415-424.
4. J. Bico, C. Tordeux and D. Quere, *Europhysics Letters*, 2001, **55**, 214-220.
5. M. Miwa, A. Nakajima, A. Fujishima, K. Hashimoto and T. Watanabe, *Langmuir*, 2000, **16**, 5754-5760.
6. A. B. D. Cassie and S. Baxter, *Transactions of the Faraday Society*, 1944, **40**, 0546-0550.